Tropical water vapor variations during the 2006–2007 and 2009–2010 El Niños: Satellite observation and GFDL AM2.1 simulation

Hanii Takahashi,[1] Hui Su,[2] Jonathan H. Jiang,[2] Zhengzhao Johnny Luo,[3] Shang-Ping Xie,[4,5] and Jan Hafner[5]

Received 16 January 2013; revised 26 June 2013; accepted 24 July 2013.

[1] Water vapor measurements from Aura Microwave Limb Sounder (MLS, above 300 hPa) and Aqua Atmospheric Infrared Sounder (AIRS, below 300 hPa) are analyzed to study the variations of moisture during the 2006–2007 and 2009–2010 El Niños. The 2006–2007 El Niño is an East Pacific (EP) El Niño, while the 2009–2010 El Niño is a Central Pacific (CP) El Niño or El Niño *Modoki*. Results show that these two types of El Niño events produce different patterns of water vapor anomalies over the tropical ocean, approximately resembling the cloud anomalies shown in Su and Jiang (2013). Regression of water vapor anomalies onto the Niño-3.4 SST for the A-Train period shows a clear "upper tropospheric amplification" of the fractional water vapor change, i.e., the ratio of the change in specific humidity to the layer-averaged specific humidity. Furthermore, tropical water vapor anomalies in different circulation regimes are examined. It is shown that the variations of water vapor during the 2006–2007 El Niño are mainly controlled by the thermodynamic component, whereas both dynamic and thermodynamic components control the water vapor anomalies during the 2009–2010 El Niño. GFDL AM2.1 model simulations of water vapor and cloud anomalies for the two El Niños are compared with the satellite observations. In general, the model approximately reproduces the water vapor anomalies on both zonal and meridional planes but it produces too strong a cloud response in the mid- and lower troposphere. The model fails to capture the dynamic component of water vapor anomalies, particularly over the Indian Ocean.

Citation: Takahashi, H., H. Su, J. H. Jiang, Z. J. Luo, S.-P. Xie, and J. Hafner (2013), Tropical water vapor variations during the 2006–2007 and 2009–2010 El Niños: Satellite observation and GFDL AM2.1 simulation, *J. Geophys. Res. Atmos.*, *118*, doi:10.1002/jgrd.50684.

1. Introduction

[2] El Niño-Southern Oscillation (ENSO) is characterized by anomalous sea surface temperature (SST) in the eastern-to-central equatorial Pacific. It plays an important role in interannual variability of global climate through strong teleconnection. Since a new type of El Niño named the Central Pacific (CP) El Niño or El Niño *Modoki* was discovered, much effort has been made to examine the mechanism of CP El Niño, which exhibits a unique horseshoe warming pattern in the equatorial central Pacific extending toward the subtropics [*Ashok et al*., 2007; *Kao and Yu*, 2009]. A number of papers have pointed out that the impacts of this new type of El Niño over many parts of the globe are different from those of the canonical Eastern Pacific (EP) El Niño [*Latif et al*., 1997; *Ashok et al*., 2007; *Kao and Yu*, 2009; *Kug et al*., 2009; *Weng et al*., 2007; *Weng et al*., 2009; *Kim et al*., 2009]. Furthermore, *Kao and Yu* [2009] emphasized that the EP El Niño is a cyclic oscillation coupled with basin-wide thermocline and surface wind variations and has strong teleconnection with the tropical Indian Ocean, while the CP El Niño is an event associated with atmospheric forcing rather than changes in thermocline and has stronger teleconnection with the Southern Indian Ocean.

[3] The variations of cloudiness and cloud radiative forcing (CRF) during ENSO have been examined extensively [*Ramanathan and Collins*, 1991; *Zhang et al*., 1996; *Cess et al*., 2001; *Allan et al*., 2002]. A recent study by *Su and Jiang* [2013] (hereinafter referred to as SJ13) showed that the variations of tropical cloud vertical structure, CRF, and circulation during the 2006–2007 El Niño (moderate EP El Niño) are strikingly different from those of the 2009–2010 El Niño (strong CP El Niño). In terms of the tropical mean, for example, during the 2006–2007 El Niño, the intensity of tropical circulation (primarily the Walker circulation)

[1]Program in Earth and Environmental Sciences, Graduate Center, CUNY, New York, New York, USA.
[2]Jet Propulsion Laboratory, California Institute of Technology, Pasadena, California, USA.
[3]Department of Earth and Atmospheric Sciences and CREST Institute, City College of New York, CUNY, New York, New York, USA.
[4]Scripps Institution of Oceanography, University of California, San Diego, La Jolla, California, USA.
[5]International Pacific Research Center, and Department of Meteorology, SOEST, University of Hawai'i at Manoa, Honolulu, Hawaii, USA.

Corresponding author: H. Su, Jet Propulsion Laboratory, California Institute of Technology, 4800 Oak Grove Dr., Pasadena, CA 91109, USA. (Hui.Su@jpl.nasa.gov)

2169-897X/13/10.1002/jgrd.50684

becomes weaker, with the amount of mid-high (low) clouds increases (decreases), and a net cloud warming effect (0.2–0.5 W/m^2) is found. On the contrary, during the 2009–2010 El Niño, the intensity of tropical circulation (primarily the Hadley circulation) becomes stronger, with the amount of mid-high (low) clouds decreases (increases), and a net cloud cooling effect (0.6–0.7 W/m^2) is found. Moreover, SJ13 found that the variations of clouds and circulation during the two El Niños are more dominated by the magnitude than the pattern of anomalous SST. To further identify the different characteristics of the two types of El Niños, it is of interest to investigate variations in water vapor associated with the two ENSO events.

[4] Water vapor is an important component of the atmosphere. It is a highly variable trace constituent of the atmosphere; it is also the primary contributor to the atmospheric greenhouse effect [*IPCC*, 2007]. When water vapor condenses, a warming occurs due to the release of latent heat. In deep convection, the warm air parcel rises and develops into large cumulonimbus clouds and then detrains at the upper troposphere. As such, water vapor plays an important role in energy balance and subsequently affects atmospheric circulation. As the CP El Niño has been more frequent than the EP El Niño since the 1980s [*Latif et al*., 1997; *Ashok et al*., 2007; *Kao and Yu*, 2009; SJ13], it is useful to document how the atmospheric moisture changes during the CP El Niño differ from those during the EP El Niño. The primary purpose of this paper is to reveal the variations of the vertical distributions of water vapor and its relation to clouds during the two different types of El Niño events. The data used are water vapor profiles from the Atmospheric Infrared Sounder (AIRS) for the lower-to-middle troposphere (LT/MT) and from the Microwave Limb Sounder (MLS) for the upper troposphere to lower stratosphere (UT/LS). In parallel to SJ13, vertical distributions of water vapor in meridional and zonal planes during the 2006–2007 and 2009–2010 El Niños are analyzed first. Next, using the conditional sampling approach as in *Bony et al*. [2004], we examine how water vapor variations are connected to changes in large-scale circulation. We also compare the water vapor variations with those of clouds represented by CloudSat/CALIPSO cloud fraction (CFr) anomalies and CloudSat cloud water content (CWC) anomalies shown in SJ13.

[5] Moreover, Geophysical Fluid Dynamics Laboratory (GFDL) AM2.1 model simulations of water vapor and clouds are examined and compared with the satellite observations. We evaluate how realistically the two El Niño events are simulated in the model and diagnose the discrepancies between the model simulation and the observations. The vertical structures of water vapor and clouds are important for radiation balance and thus climate. Climate models' skills in simulating the vertical structure of clouds and water vapor are far from satisfactory [*Jiang et al*., 2012; *Su et al*., 2013; *Tian et al*., 2013], while the model simulated interannual anomalies of water vapor and clouds have not been rigorously tested. At the time of the analysis, only GFDL AM2.1 was available to us to conduct a multiyear simulation driven by the observed SST that included the 2006–2007 and 2009–2010 El Niños. The comparison of model results with the observations helps to identify model weaknesses and guide future model improvements. Our diagnosis of model errors helps to identify the sensitive geographical regions for the tropical-mean interannual anomalies and the important teleconnection processes that determine the tropical-mean water vapor response during El Niños.

[6] Finally, we regress the water vapor anomalies at each pressure level onto the Niño-3.4 SST (5°S–5°N and 190–240°E) using the data over the entire observational period of Aqua and Aura to extract the general features of water vapor response to ENSO SST forcing (focusing on the vertical variation of water vapor anomalies), and to quantify the average magnitude of water vapor response to the SST warming. In this paper, we focus on the ENSO responses over tropical ocean. The interannual anomalies over land are deferred to the future.

[7] The rest of the paper is organized as follows. Section 2 describes the analysis methods and data used. Results and interpretations are presented in section 3. Section 4 summarizes the study.

2. Data and Analysis Methods

[8] AIRS on Aqua was launched in 2002, which carries a nadir-scanning sounder together with infrared and microwave retrievals [*Aumann et al*., 2003]. It has 2378 IR channels in the spectral range from 3.74 to 15.4 **μm** and its footprint is approximately 13.5 km at nadir. The AIRS provides rich and accurate information about the atmosphere (water vapor, temperature, and minor gases such as CO_2, CO, CH_4, O_3, and SO_2) with the purpose of improving weather forecasting and studying water and energy cycle [*Le Marshall et al*., 2005]. *Chahine et al*. [2006] provide a detailed overview of the AIRS data. We use AIRS version 5, Level 3 water vapor product AIRX3STD [*Olsen et al*., 2007] whose spatial resolution is 50 km, but aggregated on $1° \times 1°$ (longitude × latitude) grids. The estimated water vapor uncertainly is 25% in the tropics and the usable altitude range over the ocean is from 1000 hPa to 300 hPa [*Jiang et al*., 2012].

[9] MLS on Aura was launched in 2004, designed to observe chemical constituents from the UT/LS by thermal emission from the atmospheric limb centered near 118, 190, 240, and 640 GHz, and 2.5 THz [*Waters et al*., 2006]. It produces vertical profiles of atmospheric water vapor, temperature, cloud ice, and chemical tracers such as CO and O_3, etc. Its retrievals are horizontally spaced by 167 km along the orbital track [*Waters et al*., 2006], and the detailed retrieval methodology is described in *Livesey et al*. [2006]. We use MLS Version 3, Level 2 water vapor product [*Livesey et al*., 2011]. The vertical resolutions of the MLS water vapor are ~3.0 km, with 20% uncertainties at 215 hPa and 10% at 100 hPa [*Read et al*., 2007; *Jiang et al*., 2010]. To ensure best quality of data, we use the water vapor from AIRS at and below the 300 hPa pressure level and water vapor from MLS above the altitude of 300 hPa. For combined AIRS and MLS water vapor profiles, we use the data from 2004 to 2011, including seven DJFs.

[10] For cloud profiles, the CloudSat radar and Cloud-Aerosol Lidar and Infrared Pathfinder Satellite Observations (CALIPSO) [*Winker et al*., 2003] combined CFr from 2B-GEOPROF-LIDAR are used together with the CWC produced by SJ13 from CloudSat Level 2BCWC-RO. The CloudSat and CALIPSO were launched in April 2006

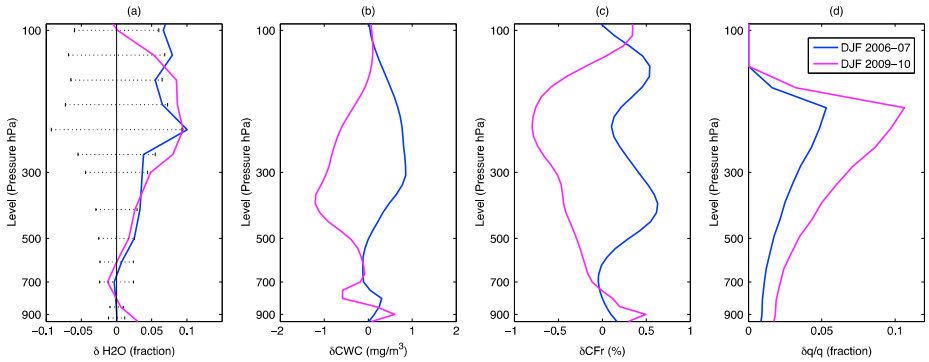

Figure 1. Tropical-mean (30°S–30°N) anomalies of water vapor fraction (a) with the error bars (std) centered at zero, cloud water content (b), cloud fraction (c), and hypothetical water vapor (H_2O) fraction changes under "constant relative humidity" assumption (see text for details) (d) for two El Niños at different pressure levels. Blue line represents during the 2006–2007 El Niño and magenta line represents during the 2009–2010 El Niño.

[*Stephens et al*., 2008]. The former satellite carries a 94 GHz cloud profiling radar (CPR) [*Im et al*., 2006] that is sensitive to both cloud-size and precipitation-size particles and the latter is sensitive to optically thin clouds, which CPR might not capture. Combined CloudSat and CALIPSO measurements thus offer effective global survey of cloud vertical profile from deep convection to thin high clouds. The footprint of these data is 1.7 km along track and 1.3 km cross track, and the vertical resolution is 480 m [*Stephens et al*., 2002].

[11] Aqua, Aura, CALIPSO, and CloudSat are all members of the A-Train constellation [*L'Ecuyer and Jiang*, 2010], flying in a sun-synchronous orbit with an equator crossing time around 1:30 am/pm. Aqua leads Aura by about 8 min [*Stephens et al*., 2002]. CALIPSO follows Aqua by 1–2 min and CloudSat by 10–15 s [*Sun-Mack et al*., 2007].

[12] Following the satellite data analysis, we examine the simulated water vapor responses to the two El Niños in the GFDL AM2.1 model driven by the observed SST from 2005 to 2012. GFDL AM2.1 is an atmosphere-only model. It has high skills in reproducing dynamical response to tropical SST variability (including ENSO) [*Lau et al*., 2006] and consistently ranked among the top models with regard to the skills in simulating tropical variability [*Annamalai et al*., 2007]. *Su et al*. [2011] evaluated the cloud simulations in one version of AM2 for the period of October 2006 to September 2007 using CloudSat data. However, the AM2.1 performance for the vertical structures of water vapor and clouds during the two recent El Niños has not been examined. The horizontal resolution is $2.5° \times 2°$ (longitude × latitude). It has 24 vertical levels: the lowest level is about 30 m above the surface, nine full levels are in the lowest 1.5 km above the surface, and five levels are in the stratosphere with the highest level at about 3 hPa [*Anderson et al*., 2004]. This model uses 3 hourly intervals for atmospheric radiation and 0.5 hourly intervals for other atmospheric physics. A diurnal cycle of insolation is included in this model [*Delworth et al*., 2006]. The model has a moist bias in the upper tropospheric relative humidity compare to Television and Infrared Observation Satellite (TIROS) Operational Vertical Sounder [*Anderson et al*., 2004].

[13] As water vapor distribution strongly depends on temperature and altitude (it decreases by four orders of magnitude from the surface to the tropical tropopause), we mainly use water vapor fractional change (%), that is, the ratio of the change in specific humidity to the layer-averaged specific humidity, rather than changes in actual water vapor amounts (ppmv). Also, as El Niño warming is generally maximized in boreal winter, we focus on analyzing the water vapor anomalies averaged for December, January, and February (DJF). We use the methodology introduced by *Bony et al*. [2004] to understand the linkage between the water vapor distribution and large-scale circulation. Fundamentally, water vapor and convection are controlled by thermodynamics (e.g., Clausius-Clapeyron (CC) relationship) and dynamics (e.g., rising or sinking motion), respectively. From a large-scale perspective, both dynamics and thermodynamics play an important role in affecting clouds and water vapor [*Bony et al*., 2004]. In this framework, $\boldsymbol{\omega}_{500}$, midtropospheric vertical pressure velocity at 500 hPa, is used as a proxy of local dynamic condition, and water vapor is treated as a function of $\boldsymbol{\omega}_{500}$ weighted by the probability density function of each $\boldsymbol{\omega}_{500}$ regime. We use the following equation:

$$\delta(Q_\omega P_\omega) = Q_\omega \ \delta P_\omega + P_\omega \ \delta Q_\omega + \delta Q_\omega \ \delta P_\omega \qquad (1)$$

where Q_ω is the water vapor in a regime of the value ω and P_ω is the probability distribution function of the regime ω. We use $\boldsymbol{\omega}_{500}$ from the European Centre for Medium-Range Weather Forecasts (ECMWF) ERA-interim reanalysis data set and define 20 bins of $\boldsymbol{\omega}_{500}$ with the bin interval of 10 hPa/day. In such a framework, anomalies of water vapor ($\delta(Q_\omega P_\omega)$) can be decomposed into a dynamic component ($Q_\omega \ \delta P_\omega$), a thermodynamic component ($P_\omega \ \delta Q_\omega$), and covariation between the two ($\delta Q_\omega \ \delta P_\omega$). Note that δQ_ω and δP_ω are anomalies from their climatological means.

3. Results

3.1. Comparison Between the 2006–2007 and 2009–2010 El Niños

3.1.1. Tropical-Mean Anomalies of Water Vapor

[14] Figure 1a shows the tropical-mean (30°S–30°N) water vapor fractional change for the two El Niños from the surface to 100 hPa with the error bars centered atzero, indicating the interannual fluctuations. In terms of tropical mean, both El Niños strongly hydrate the upper troposphere around 200

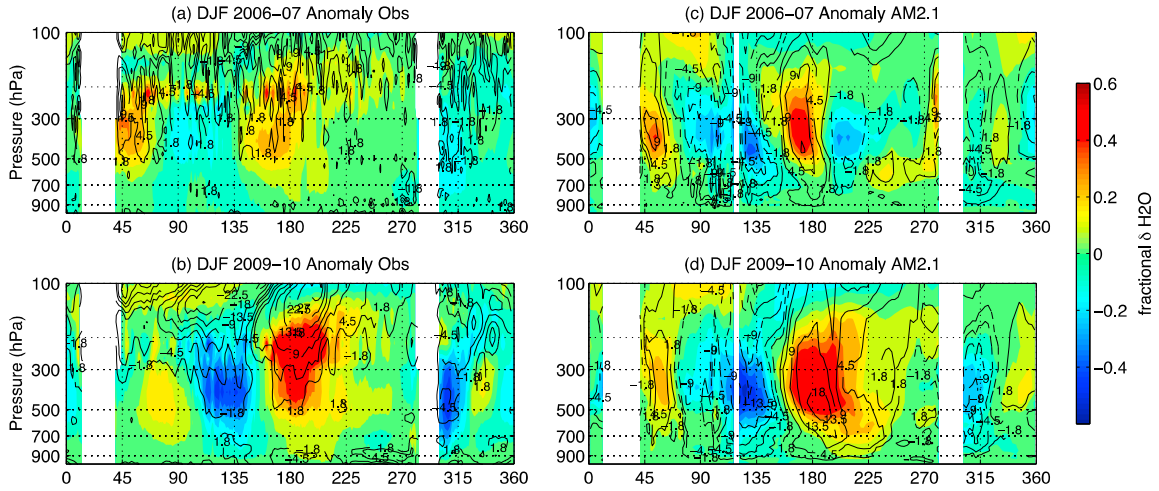

Figure 2. Longitude-height section of tropical-mean (10°S–10°N) anomalies during the DJF 2006–2007 El Niño and the DJF 2009–2010 El Niño from (a, b) satellite observations and (c, d) model simulations. Shadings represent fractional water vapor (H_2O) and contours represent cloud fraction (CFr).

hPa level (by ~10%) and slightly dehydrate around 700 hPa level. The moistening around 200 hPa exceeds one standard deviation during the 2009–2010 El Niño, close to 0.09. We call it "upper tropospheric amplification" of water vapor response to the SST warming. Considering the greenhouse effect of water vapor is mostly sensitive to the upper tropospheric water vapor [*Soden and Fu*, 1995], the amplified UT water vapor response to SST warming further underscores the importance of UT water vapor in global energy and water cycles. Earlier studies suggested that the upper tropospheric moistening is closely associated with deep convection [*Betts*, 1990; *Sun and Lindzen*, 1993; *Jiang et al*., 2004; *Su et al*., 2006; *Soden and Fu*, 1995] and the variations of UT water vapor are positively correlated with SST [*Su et al*., 2006; *Luo et al*., 2012]. However, a close examination of water vapor changes during the two El Niños reveals nonlinear relations between tropical-mean water vapor, convection (represented by clouds) and SST anomalies.

[15] During the 2009–2010 El Niño, water vapor anomalies are positive over most of the troposphere (Figure 1a) although both CWC and CFr anomalies at middle-to-upper troposphere (600 to 100 hPa) are negative (Figures 1b and 1c). The 2006–2007 El Niño, on the contrary, experienced the same sign of water vapor and cloud anomalies throughout the troposphere. Obviously, the tropical-mean water vapor changes are not simply correlated with the amount of cloud changes. Furthermore, the magnitudes of water vapor changes during the two El Niños are not proportional to the magnitude of SST anomalies, either. During the 2009–2010 El Niño, the tropical-mean SST anomalies (0.23°C) is about twice as high as that during the 2006–2007 El Niño (0.12°C), while their water vapor fractional changes do not differ by a factor of 2. Assuming tropical-mean relative humidity stays at the climatological mean value (this is the so-called "constant relative humidity" assumption) and tropospheric temperature changes following moist adiabats, the hypothetical water vapor fractional changes would look like Figure 1d, with the water vapor anomaly differences between the two El Niños proportional to the their SST anomalies. The apparent discrepancy of Figure 1d from Figure 1a motivates us to explore the water vapor changes in a detailed three-dimensional view as we discuss in the following sections. It also suggests that the "constant relative humidity" assumption does not hold on interannual time scales. Previous studies indicated that the variations in tropical or global mean relative humidity can have important effects on global hydrological cycles [e.g., *Richter and Xie*, 2008].

3.1.2. Zonal and Meridional Structures of Water Vapor Anomalies

[16] Figures 2 and 3 display the meridional-mean (10°S–10°N) and zonal-mean (0–360°E) of water vapor anomalies (in color shadings) over ocean, respectively, together with anomalies of CFr (in contours). In both figures, the left panels show the results from satellite observations, and the right panels show the model simulations.

[17] On the longitude-height cross section, the 2006–2007 El Niño (Figure 2a) produces moderately positive fractional changes of H2O over the western Indian Ocean (45–70°N) and the central Pacific (160–200°E), especially near the dateline. Over the eastern Indian (70–90°E) and the western Pacific (100–150°E), we see moderately negative moisture anomalies. In contrast, the 2009–2010 El Niño (Figure 2b) has a widespread strong moistening across the central to eastern Pacific with a strong hydration near the dateline at 300–200 hPa. Strong negative anomalies are observed over the western Pacific and maritime continents, peaking at 400 hPa. Positive anomalies occur over the eastern Indian Ocean. For both El Niño events, the pattern of water vapor anomalies is similar to that of CFr; however, some differences are outstanding during the 2009–2010 El Niño. First, the peak heights of both negative and positive water vapor anomalies are lower than those of CFr. Second, while water vapor has positive anomalies over the eastern Indian, such positive anomalies are not observed in CFr. We have also compared the water vapor anomalies to CWC anomalies during the 2009–2010 DJF and found that negative CWC anomalies are observed over most of the eastern Indian with a very narrow band of positive anomalies (SJ13). The balance between the moistening due to the evaporation of ice

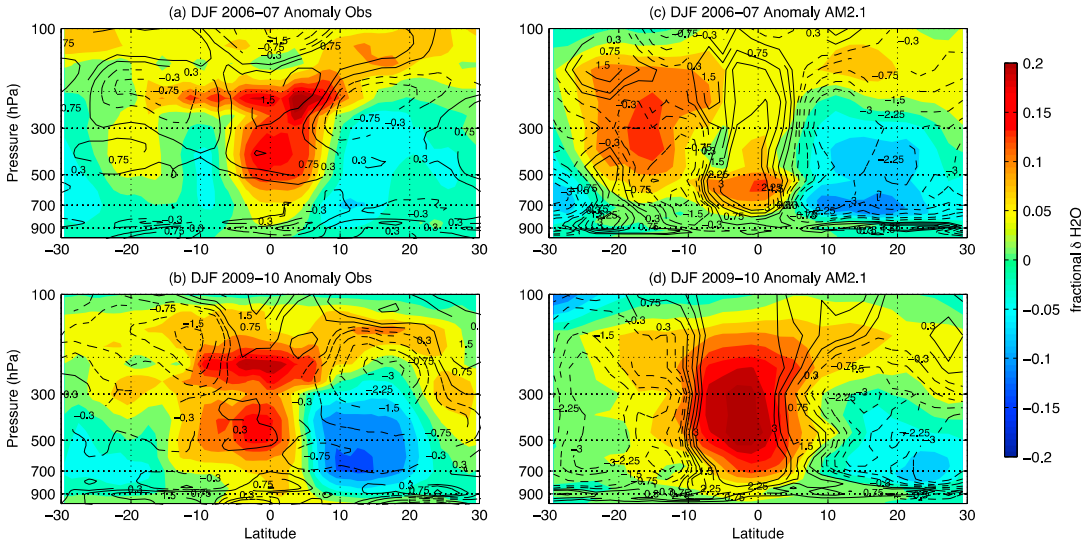

Figure 3. Latitude-height section of zonal mean (0–360°E) anomalies during the DJF 2006–2007 El Niño and the DJF 2009–2010 El Niño from (a, b) satellite observations and (c, d) model simulations. Shadings represent fractional water vapor (H_2O) and contours represent cloud fraction (CFr).

particles and the drying due to the detrainment from cold overshooting turrets is a subject that warrants further investigation.

[18] During the 2006–2007 El Niño, the difference between the satellite observation (Figure 2a) and GFDL model (Figure 2c) is outstanding in terms of amplitude. The modeled simulated alternating positive and negative moisture anomalies from the eastern Pacific (200–270°E) to the western Indian Ocean (45–70°E) are about two times stronger than the satellite observations. During 2009–2010 El Niño, the differences between the modeled and observed water vapor anomalies are mainly over the eastern Indian Ocean (45–90°E), where opposite signed anomalies are shown for the observation (Figure 2b) and the AM2.1 simulation (Figure 2d). In addition, the peak altitudes of CFr anomalies from the CloudSat/CALIPSO retrieval are much higher than the GFDL AM2.1 simulation for both El Niños, which could be mitigated by using CloudSat/CALYPSO simulator cloud fraction if available [*Su et al*., 2013]. Despite the deficiencies mentioned above, the GFDL AM2.1 captures the general pattern of water vapor responses to the ENSO SST forcing.

[19] On the latitude-height cross section, the differences in the positive water vapor anomalies between the two El Niños (Figures 3a and 3b) are not as distinctive as those in the negative anomalies. Except for the facts that anomalous moistening is slightly shifted toward the north of the equator during the 2006–2007 El Niño but toward the south of the equator during the 2009–2010 El Niño and that the boundary layer moistening is more pronounced during the 2009–2010 El Niño, the moistening of the atmosphere in response to the two El Niño events are very similar. The peak heights of increasing water vapor are found around 200 hPa in both El Niño events, which are associated with cloud ice detrainment. In contrast, the differences of anomalous drying in response to the two El Niños are rather outstanding. First, the magnitude of drying anomalies over the northern hemisphere during the 2009–2010 El Niño is much stronger than that during the 2006–2007 El Niño, especially over the 7–20° N zone. Second, the anomalous drying is widely spread over 15–30°S during the 2009–2010 El Niño, while a mixture of anomalous moistening and drying are found for the 2006–2007 El Niño. These differences are consistent with the distribution of CWC anomalies, which exhibit a broadly strong positive anomaly to the north of the equator during the 2006–2007 DJF but a narrowly distributed cloud enhancement to the south of the equator during the 2009–2010 DJF (SJ13). Negative CWC anomalies are found on the both sides of anomalous ascent, but they cover relatively very small areas (5–10°S and 10–15°N) during the 2006–2007 El Niño, compared to a much larger area (10–30°S and 5–30°N) during the 2009–2010 El Niño. However, the stronger drying over the northern than the southern hemisphere during the 2009–2010 El Niño is not consistent with the negative CWC anomalies which show equally strong magnitudes over both hemispheres (SJ13), but are in line with the negative CFr anomalies. During the 2009–2010 El Niño, the strength of the Hadley circulation increases (SJ13). The substantial drying over the northern hemisphere may be because the stronger Hadley Cell resides over the winter hemisphere, which produces anomalously strong sinking motion over the subtropics in the northern hemisphere. Water vapor and CFr anomalies appear to be more sensitive to the variation in the Hadley circulation than the CWC anomalies.

[20] The zonal-mean water vapor anomalies are very different between the satellite observation (Figures 3a and 3b) and the GFDL AM2.1 simulation (Figures 3c and 3d). The difference in the amplitude of negative anomalies is significant in the Northern Hemisphere, where AM2.1 simulated water vapor anomalies are much drier in the lower to middle troposphere than the satellite observation for the 2006–2007 El Niño but reversely for the 2009–2010 El Niño. The differences around the equator and in the Southern Hemisphere are also evident: during the 2006–2007 El Niño, GFDL AM2.1 underestimates the moistening at the equator but overestimates it between 10–20°S; during the 2009–2010 El Niño, AM2.1 overestimates the midtropospheric moistening around the equator but underestimates the lower tropospheric drying between 10 and 20°N and between 20 and 30°S. In addition, the observed "upper tropospheric amplification"

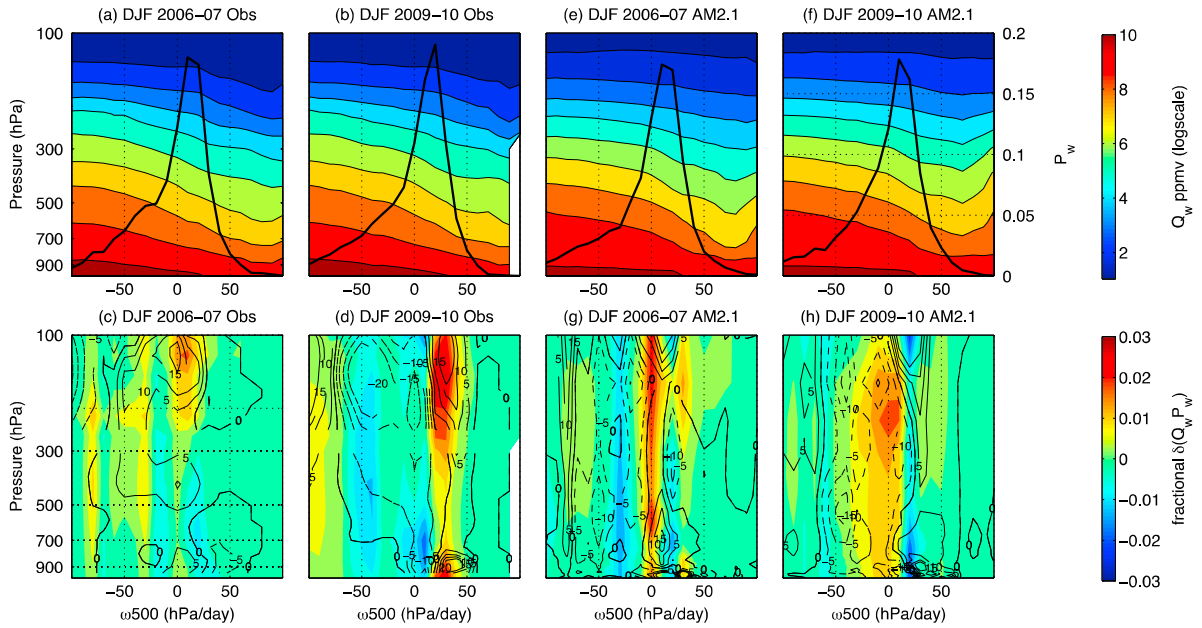

Figure 4. (a, b, e, and f) Water vapor sorted as a function of vertical pressure velocity at 500 hPa, $\boldsymbol{\omega}_{500}$ and (c, d, g, and h) fractional water vapor (H_2O) anomalies as a function of $\boldsymbol{\omega}_{500}$ weighted by probability density function of each regime during the DJF 2006–2007 El Niño (left panel) and during the DJF 2009–2010 El Niño (right panel). The solid curves in Figures 4a, 4b, 4e, and 4f are probability density function of each regime. Line contours in Figures 4c, 4d, 4g, and 4h represent cloud fraction (CFr) (unit: 10^{-3} %). Figures 4a–4d are from satellite observations and Figures 4e–4h are from model simulations.

of moistening at the equatorial zone is not simulated in the model. The lower altitudes of peak moistening could be related to the lower altitude of peak convective detrainment indicated by the maximum CFr anomalies. Moreover, AM2.1 strongly overestimates the amplitude of CFr anomalies, by a factor of 10 in some places. It might not be very fair to demand the model to reproduce the zonal mean cloud anomalies because the zonal mean anomalies result from the compensation of large regional anomalies (Figures 3c and 3d) and are one order of magnitude smaller than the regional anomalies such as those shown in Figure 2.

3.1.3. Water Vapor Anomalies Sorted by Large-Scale Circulation

[21] Figure 4 shows the water vapor profiles and their anomalies sorted by the 20 bins of $\boldsymbol{\omega}_{500}$ with a bin interval of 10 hPa/day for the two El Niños in the observations and in AM2.1 simulations. In general, water vapor at all levels increases monotonically with decreasing $\boldsymbol{\omega}_{500}$ (except at the strongly descending regime, where the occurrence frequency is close to zero). The modeled 3 month (DJF) mean water vapor profiles appear to be moister than the observed at all vertical heights, but the variation of water vapor with $\boldsymbol{\omega}_{500}$ is captured. Both the 2006–2007 and 2009–2010 El Niños have anomalous moistening over strongly ascending regimes ($\boldsymbol{\omega}_{500} < -75$ hPa/day). Over moderately descending regimes ($20 < \boldsymbol{\omega}_{500} < 50$ hPa/day), both the 2006–2007 and 2009–2010 El Niños have anomalous moistening above 300 hPa; however, the 2006–2007 El Niño has anomalous drying and the 2009–2010 El Niño has strong anomalous moistening below 300 hPa. In between these two regimes ($-75 <$ $_{500} < 20$ hPa/day), the 2009–2010 El Niño has strong drying anomalies, whereas the 2006–2007 El Niño has a mixture of both moistening and drying anomalies. Overall, the pattern of water vapor anomalies is similar to that of CFr anomalies in contours, especially during the 2009–2010 El Niño (Figure 4d). The exception is found during the 2006–2007 El Niño over the strongly ascending regimes ($\boldsymbol{\omega}_{500} < -75$ hPa/day) where water vapor has positive anomalies, but CFr has negative anomalies (Figure 4c). In contrast to the similarity between the model simulations and the observations in terms of the seasonal mean water vapor profiles, the anomalies of water vapor in the $\boldsymbol{\omega}_{500}$ regimes show large discrepancies from the observations. For the 2006–2007 El Niño, the model overestimates the moistening and drying anomalies in the intermediate circulation regime ($-50 < \boldsymbol{\omega}_{500} < 10$ hPa/day). For the 2009–2010 El Niño, the model simulates a broad anomalous moistening in this intermediate circulation regime, opposite to the observed anomaly.

[22] Figure 5 shows the three components of the fractional water vapor anomalies as a function of large-scale circulation regimes (Figures 4c and 4d, hereafter referred to as the total anomalies): the dynamic component ($\sum(Q_\omega \delta P_\omega)$, a and b), thermodynamic component ($\sum(P_\omega \delta Q_\omega)$, c and d), and covariation ($\sum(\delta Q_\omega \delta P_\omega)$, e and f), which is small compared to the first two components. The AM2.1 simulations are shown together with the observations.

[23] Comparing the two El Niños, the differences in the dynamic component are more outstanding than in the thermodynamic component. The patterns of the thermodynamic component for both El Niños display a ubiquitous moistening in the upper troposphere and some drying in the lower troposphere, with a peak around the maximum pdf (probability density function) of $\boldsymbol{\omega}_{500}$ at 10–20 hPa/day. The stronger UT moistening in 2009–2010 is consistent with its larger amplitude of SST warming. This confirms that the thermodynamic component is primarily controlled by SST anomalies.

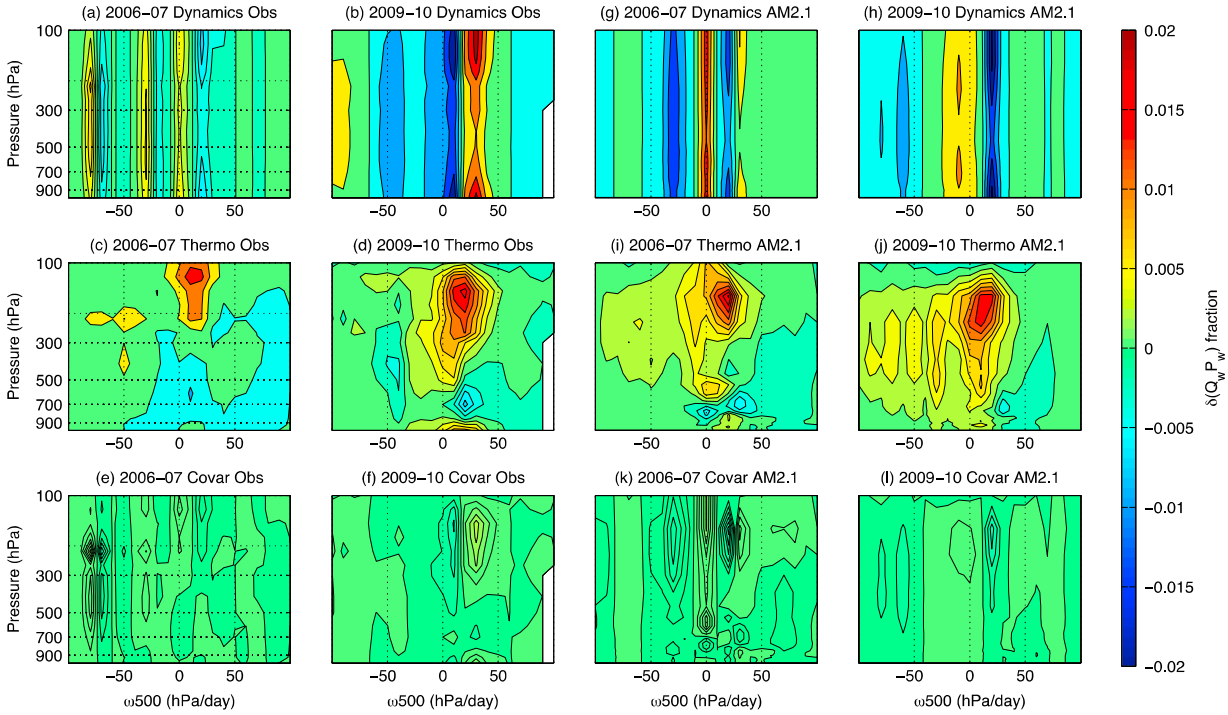

Figure 5. Three components, (a, b, g, and h) dynamic component, (c, d, i, and j) thermodynamic component, and (e, f, k, and l) covariation, of fractional water vapor anomalies changes as a function of $\boldsymbol{\omega}_{500}$ during the DJF 2006–2007 El Niño and during the DJF 2009–2010 El Niño. Figures 5a–5f are from satellite observations and Figures 5g–5l are from model simulations.

However, the distributions of the dynamic component for each El Niño are qualitatively different. In 2006–2007, a complicated pattern of alternating positive and negative anomalies is shown (Figure 5a), while a clear "sandwiched" positive-negative-positive pattern is found (Figure 5b) in 2009–2010 with much stronger amplitudes. The dynamic component is driven by the pdf change of $\boldsymbol{\omega}_{500}$. The patterns in Figure 5a and 5b are manifestation of the effects of large-scale circulation changes on the water vapor profiles. As elaborated in SJ13, the Hadley Circulation strengthens during the 2009–2010 El Niño, producing increased moisture at the strongly ascending and descending regimes and decreased moisture at the intermediate regime. During the 2006–2007 El Niño, the Walker Circulation weakens. The pdf changes of $\boldsymbol{\omega}_{500}$ yield an increase of moisture in the moderate circulation regimes accompanied by small-amplitude alternating anomalies in nearby circulation regimes. This dynamic component for 2006–2007 is different from that in SJ13, because the climatological $\boldsymbol{\omega}_{500}$ distribution is based on the 8 years (2004–2011) instead of the 4 years (2006–2010) in SJ13.

[24] Table 1 shows the sum of the total anomalies and its three components over all vertical levels and over the tropical oceans for the two El Niños. During the 2006–2007 El Niño, the thermodynamic component (0.46) far outweighs the dynamic component (0.047) on the tropical mean. The pattern of the total anomalies (Figure 4c) is also similar to the thermodynamic component (Figure 5c). The 2009–2010 El Niño seems to draw a different story: although the thermodynamic component (0.65) is larger than dynamic component (−0.096) on the tropical mean, the pattern of the total anomalies (Figure 4d) is similar to the pattern of the dynamic component (Figure 5b). These results suggest that the tropical-mean water vapor anomaly is mostly determined by the thermodynamic factor (e.g., the temperature control), while local water vapor anomalies are strongly influenced by the dynamic factor such as ascent or descent anomalies. During the 2006–2007 El Niño, the large-scale circulation changes are of weaker magnitude (SJ13) than during the 2009–2010 El Niño. Therefore, the water vapor anomalies are mostly controlled by the thermodynamic factor during the 2006–2007 El Niño, but they are dependent on both dynamic and thermodynamic changes during the 2009–2010 El Niño.

[25] Examining the water vapor simulations in the large-scale circulation regimes reveals more clearly the differences between the satellite observations and model simulations. Despite the quantitative differences in the amplitude of moistening anomalies, the thermodynamic components simulated in AM2.1 are similar to the observed, because they are primarily driven by observed SST. On the other hand, the model simulated dynamic components deviate

Table 1. The Sum Over All Vertical Levels and Over the Tropical Oceans for Fractional Water Vapor (H_2O) Anomalies in the Different Circulation Regimes (δ(QωPω)) and the Dynamic Component (QωδPω), Thermodynamic Component (PωδQω), and Covariation (δQωδPω) During 2006–2007 and 2009–2010 El Niños

	Satellite Observation		GFDL Model Simulation	
Sum	2006–2007 El Niño	2009–2010 El Niño	2006–2007 El Niño	2009–2010 El Niño
δ(QωPω)	0.51	0.55	−0.26	−1.21
QωδPω	0.047	−0.096	−0.202	−0.036
PωδQω	0.46	0.65	−0.08	−1.194
δQωδPω	0.0025	0.0020	−0.019	−0.02

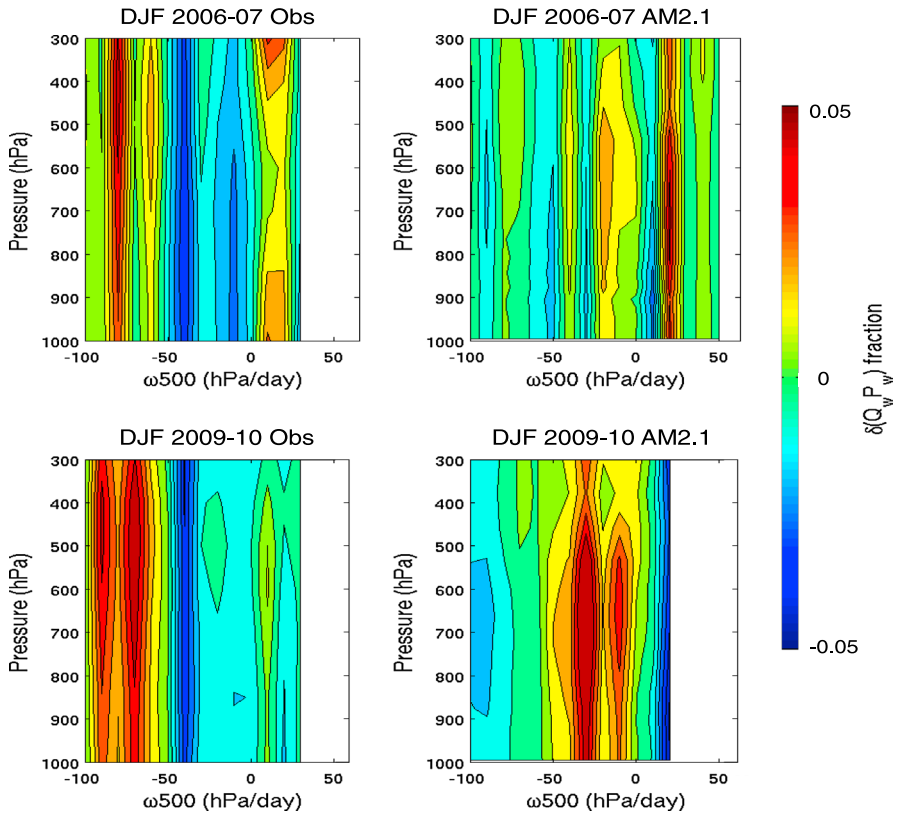

Figure 6. Same as (left) Figures 4c and 4d and (right) Figures 6c and 6d but limited the region over the Indian Ocean.

from the observations significantly for both El Niños. The model overestimates the dynamic changes in all circulation regimes for the 2006–2007 El Niño. In the moderate ascending regime around −25 hPa/day of ω_{500}, the sign of anomaly is opposite to the observed. For the 2009–2010 El Niño, the model simulated dynamic component is nearly a reversed "sandwich" compared to the observed. Our analysis suggests that the dynamic component associated with the interannual changes of large-scale circulation is difficult to simulate, while the temperature-driven thermodynamic component is relatively easy to reproduce as the model is driven by the observed SST.

[26] On the tropical mean, the fractional water vapor anomalies in the different circulation regimes show anomalous moistening in both El Niños; however, anomalous drying is found from the AM2.1 model simulations, especially during the 2009–2010 El Niño (Table 1). During the 2006–2007 El Niño, the model simulated dynamic component (−0.202) outweighs the thermodynamic component (−0.080), and the patterns of the total anomalies (Figure 4g) are similar to the dynamic component (Figure 5g), which is inconsistent with the satellite observation. During the 2009–2010 El Niño, on the other hand, the model simulated thermodynamic component (−1.194) outweighs the dynamic component (−0.036) and the patterns of the total anomalies are similar to the dynamic component (Figure 5h), which is consistent with the satellite observation but with a reversed sign of anomalies.

[27] We analyze further the contribution of each ocean basin to the total anomalies and find that the discrepancy between the satellite observation and model simulation predominantly lies in the Indian Ocean. Figure 6 shows the same analysis applied to the Indian Ocean only. The model simulation shows nearly opposite anomalies in ascending regimes to the observation for both El Niño events. ENSO excites strong teleconnection into the tropical Indian Ocean where a basin-wide warming usually occurs during El Niño [*Klein et al*., 1999; *Du et al*., 2009]. Thus, the Indian Ocean experiences local SST forcing and remote ENSO teleconnection. Atmospheric GCMs tend to respond excessively to local Indian Ocean SST anomalies [*Kumar and Hoerling*, 1998], leading to errors in tropical-mean cloud and water vapor anomalies. To understand why the model fails to reproduce the water vapor response over the Indian Ocean, sensitivity model experiments are needed and more El Niño events should be examined.

3.2. Regression Analysis of Water Vapor Anomalies on the Niño-3.4 SST

[28] Since the two El Niños examined might not represent averaged water vapor response to the SST forcing, we expand the analysis to the 8 year AIRS/MLS water vapor over the entire overlapped Aqua/Aura period (2004–2011). Regression of water vapor mixing ratio anomalies (Figure 7, Left) and relative humidity (RH) anomalies (Figure 7, Right) onto the Niño-3.4. SST (5°S–5°N and 190–240°E) is conducted. The vertical profiles of regression coefficients for the fractional water vapor (Figure 8, Left) and RH (Figure 8, Right) are further examined over the western Pacific (10°S–10°N and 100–150°E) and the central Pacific (10°S–10°N and

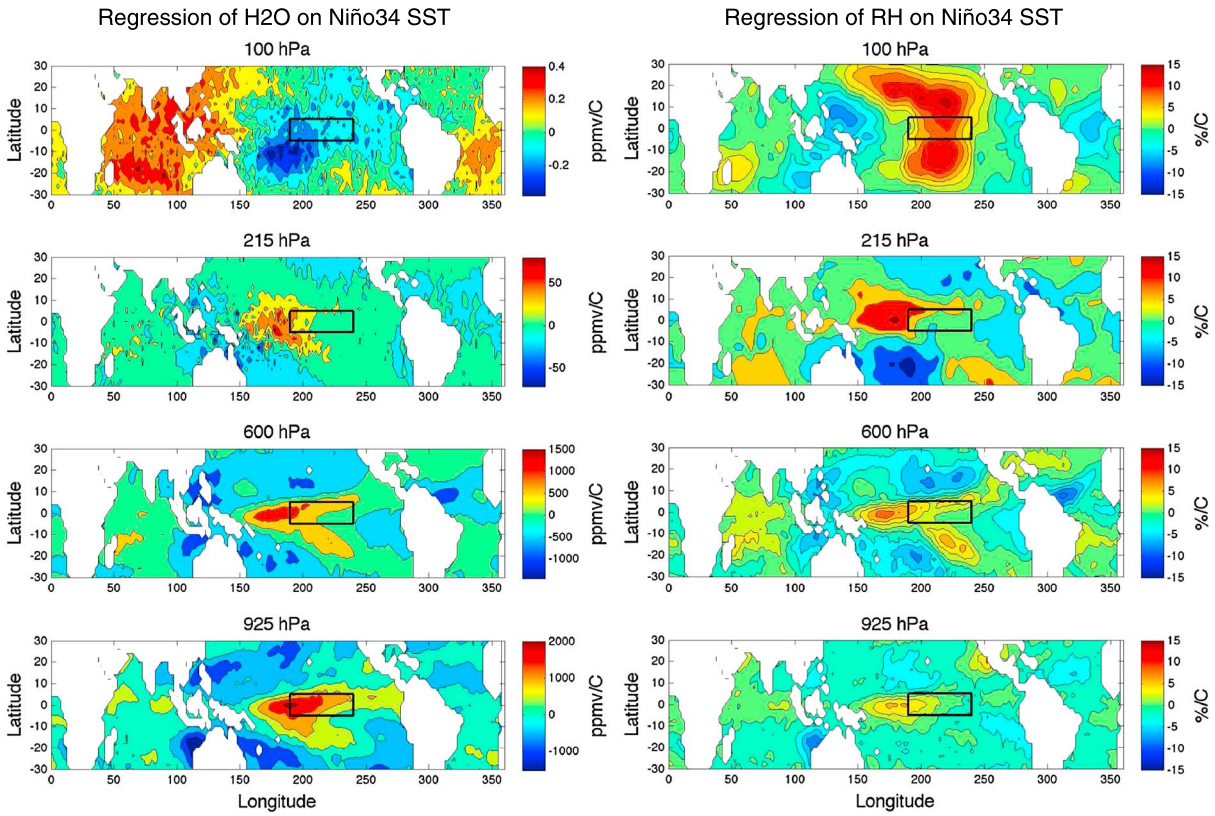

Figure 7. Regressions of (left) water vapor mixing ratio anomalies [ppmv/C] and (right) relative humidity anomalies [%/C] onto the Niño-3.4 SST at four vertical levels. Black box is the area of Niño-3.4. SST (5°S–5°N and 190–240°E).

160–200°E) separately, where the most pronounced negative and positive cloud anomalies are observed, respectively, during the two ENSO events, together with those for the whole tropics (30°S–30°N).

[29] The spatial maps (Figure 7) show that water vapor and Niño-3.4 SST are positively correlated over the central Pacific (except at 100 hPa) and negatively correlated to the northwest and southwest of the central Pacific, forming a "horse-shoe" pattern. Spatial distributions of regression for water vapor mixing ratio and RH are broadly similar in the LT/MT (900–215 hPa). However, they look very different at 100 hPa. This is because near the tropopause, water vapor and RH variations are highly controlled by temperature, which produces an opposite sign of anomaly compared to the levels below. From Figure 8, we can clearly see the "upper tropospheric amplification" of water vapor response to SST warming, which is consistent with the two particular El Niños, especially over the central Pacific. This confirms

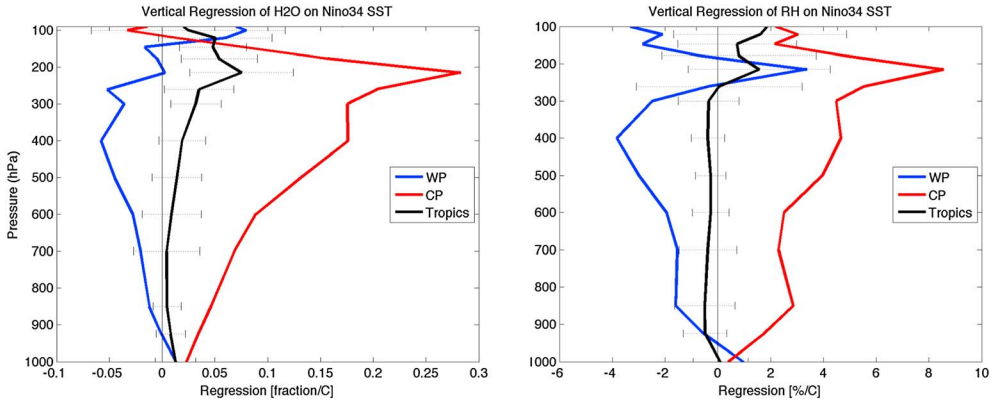

Figure 8. Regression of the (left) fractional change in water vapor and (right) relative humidity anomalies over tropics (black line: 30°S–30°N), western Pacific (blue line: 10°S–10°N and 100–150°E) and over central Pacific (read line: 10°S–10°N and 160–200°E). The error bars correspond to 1−σ confidence interval of regression fits.

that although water vapor is more abundant at the surface, the tropical upper troposphere moistens up at a faster rate in the fractional sense than the surface during El Niños. *Su et al*. [2006] pointed out that the rate of UT water vapor increase with SST is about three times of that implied by the CC equation (7%/C). A previous study by *Chuang et al*. [2010] showed the fractional increase rate of water vapor with SST (q^{-1}dq/*dSST*) is ~0.18/C at 250 hPa when q is averaged over whole tropics and *SST* is averaged over convective regions by using AIRS data. *Luo et al*. [2012] analyzed MOZAIC (Measurement of Ozone and Water Vapor by Airbus In-Service Aircraft) data and found that the q^{-1}dq/*dSST* in the vicinity of deep convective outflow is ~0.16/C at 262 hPa and ~0.18/C at 238 hPa. The fractional increase rate of water vapor with Niño-3.4. SST (q^{-1}dq/*dSST3.4*) is the highest over the central Pacific around 200 hPa (0.28/C), which is much higher than those from *Chuang et al*. [2010] and *Luo et al*. [2012]. On the other hand, the western Pacific experiences anomalous drying over most of the troposphere, which partially compensates the moistening in the central Pacific, leading to rather small changes in the tropical-mean water vapor (within one standard deviation of regression fitting), except in the UT. The tropical-mean relative humidity regression with Niño-3.4 SST is also insignificant with a relatively large amplitude in the UT.

4. Summary and Discussion

[30] This study examines the vertical distribution of water vapor anomalies during the two different types of El Niños, EP and CP El Niños, following the study of SJ13. SJ13 showed that tropical-mean cloud responses to the two El Niño are nearly opposite in terms of anomalous cloud vertical profiles and TOA (top-of-atmosphere) cloud radiative forcing. The large-scale circulation changes are also drastically different during the two El Niños (SJ13). In this study, we compare the vertical structures of water vapor anomalies during the two El Niños in both conventional geographical space and large-scale circulation regimes. We further decompose the water vapor anomalies into the dynamic and thermodynamic components to delineate the physical mechanisms that drive the water vapor changes. GFDL AM2.1 model simulations of water vapor and CFr are examined and compared with the satellite observations. Besides analyzing the two El Niños, we also conduct a regression analysis of the water vapor and relative humidity profiles onto the Niño-3.4 SST use the 8 year AIRS/MLS observations to obtain an ensemble behavior of tropical water vapor response to El Niño SST warming. The principal findings are as follows:

[31] 1. In terms of tropical mean, both El Niños strongly hydrate upper troposphere around 200 hPa and slightly dry out around 700 hPa, and lower tropospheric (1000 to 800 hPa) moistening is observed only during the 2009–2010 El Niño. Although both CFr and CWC in the middle-to-upper troposphere have negative anomalies during the 2009–2010 El Niño, water vapor anomalies are positive from 600 to 100 hPa.

[32] 2. The tropical-mean water vapor anomalies are primarily controlled by the thermodynamic component (i.e., temperature anomalies), while local anomalies are governed by both the thermodynamic and dynamic components (i.e., circulation changes). The large-scale circulation changes have a strong influence on water vapor anomalies in the 2009–2010 El Niño, but have a relatively weak role in the 2006–2007 El Niño.

[33] 3. A clear "upper tropospheric amplification" of the fractional water vapor change to El Niño is found. The rate of increase of water vapor with Niño-3.4 SST exceeds the CC value of 7%/°C and is the highest around 200 hPa (28%/°C) over the central Pacific where enhanced convection is observed. The tropical-mean relative humidity change is about 1%/°C, within the one standard deviation.

[34] 4. In terms of zonal/meridional means, GFDL AM2.1 model simulates the general patterns of water vapor response to the ENSO SST forcing. However, GFDL AM2.1 does not reproduce the strong moistening effect at 200 hPa where convective detrainment preferably occurs. Instead, the model simulated maximum CFr anomalies are found between 300 to 700 hPa level, lower than the observed maximum detrainment level.

[35] 5. The model is able to reproduce the thermodynamic component of water vapor anomalies, but does not capture the dynamic component associated with large-scale circulation changes. A critical region that dominates the model errors is found to be the Indian Ocean where the model probably overestimates the response to local SST anomalies but underestimates the teleconnection influence on regional water vapor. To better understand this deficiency, further analysis and additional model sensitivity experiments are needed to understand the model performance and improve model simulations of ENSO responses.

[36] **Acknowledgments.** HT acknowledges the JPL Graduate Fellowship program. The work was conducted at the Jet Propulsion Laboratory, California Institute of Technology, under contract with NASA. HS and JHJ thank the funding support from NASA NEWS program. HT and ZJL are supported by CloudSat-CALIPSO Science Team under grant NNX10AM31G and by SEAC4RS Science Team under grant NNX12AC13G. SPX is supported by NSF and NOAA. We greatly appreciate two reviewers' constructive comments that led to the improvement of the manuscript.

References

Allan, R. P., A. Slingo, and M. A. Ringer (2002), Influence of dynamics on the changes in tropical cloud radiative forcing during the 1998 El Niño, *J. Clim.*, *15*, 1979–1986.

Anderson, J. L., et al. (2004), The new GFDL global atmosphere and land model AM2–LM2: Evaluation with prescribed SST simulations, *J. Clim.*, *17*, 4641–4673, doi:10.1175/JCLI-3223.1.

Annamalai, H., K. Hamilton, and K. R. Sperber (2007), South Asian summer monsoon and its relationship with ENSO in the IPCC AR4 simulations, *J. Clim.*, *20*, 1071–1092.

Ashok, K., S. K. Behera, S. A. Rao, H. Weng, and T. Yamagata (2007), El Niño Modoki and its possible teleconnection, *J. Geophys. Res.*, *112*, C11007, doi:10.1029/2006JC003798.

Aumann, H. H., et al. (2003), AIRS/AMSU/HSB on the aqua mission: Design, science objectives, data products, and processing systems, *IEEE Trans. Geosci. Remote Sens.*, *41*, 253–264.

Betts, A. K. (1990), Greenhouse warming and the tropical water budget, *Bull. Am. Meteorol. Soc.*, *71*, 1464–1465.

Bony, S., J.-L. Dufresne, H. Le Treut, J.-J. Morcrette, and C. Senior (2004), On dynamic and thermodynamic components of cloud changes, *Clim. Dyn.*, *22*, 71–86.

Cess, R. D., M. Zhang, B. A. Wielicki, D. F. Young, X. Zhou, and Y. Nikitenko (2001), The influence of the 1998 El Niño upon cloud radiative forcing over the Pacific warm pool, *J. Clim.*, *14*, 2129–2137.

Chahine, M. T., et al. (2006), AIRS: Improving weather forecasting and providing new data on greenhouse gases, *Bull. Am. Meteorol. Soc.*, *87*, 911–926, doi:10.1175/BAMS-87-7-911.

Chuang, H., X. Huang, and K. Minschwaner (2010), Interannual variations of tropical upper tropospheric humidity and tropical rainy-region SST:

Comparisons between models, reanalyses, and observations, *J. Geophys. Res.*, *115*, D21125, doi:10.1029/2010JD014205.

Delworth, T. L., et al. (2006), GFDL's CM2 global coupled climate models. Part I: Formulation and simulation characteristics, *J. Clim.*, *19*, 643–674, doi:10.1175/JCLI3629.1.

Du, Y., S.-P. Xie, G. Huang, and K. Hu (2009), Role of air-sea interaction in the long persistence of El Nino-induced North Indian Ocean warming, *J. Clim.*, *22*, 2023–2038.

Im, E., S. L. Durden, and C. Wu (2006), Cloud profiling radar for the CloudSat mission, *IEEE Trans. Aerosp. Electron. Syst.*, *20*, 15–18.

IPCC (2007), Chapter 1: Historical overview of climate change science, FAQ 1.3 What is the Greenhouse Effect? http://www.ipcc.ch/publications_and_data/ar4/wg1/en/faq-1-3.html.

Jiang, J. H., B. Wang, K. Goya, K. Hocke, S. D. Eckermann, J. Ma, D. L. Wu, and W. G. Read (2004), Geographical distribution and inter-seasonal variability of tropical deep convection: UARS MLS observations and analyses, *J. Geophys. Res.*, *109*, D03111, doi:10.1029/2003JD003756.

Jiang, J. H., et al. (2010), Five-year (2004–2009) observations of upper tropospheric water vapor and cloud ice from MLS and comparisons with GEOS-5 analyses, *J. Geophys. Res.*, *115*, D15103, doi:10.1029/2009JD013256.

Jiang, J. H., et al. (2012), Evaluation of cloud and water vapor simulations in CMIP5 climate models using NASA "A-Train" satellite observations, *J. Geophys. Res.*, *117*, D14105, doi:10.1029/2011JD017237.

Kao, H. Y., and J. Y. Yu (2009), Contrasting Eastern-Pacific and Central-Pacific types of ENSO, *J. Clim.*, *22*, 615–632, doi:10.1175/2008JCLI2309.1.

Kim, H., P. J. Webster, and J. A. Curry (2009), Impact of shifting patterns of Pacific Ocean warming on North Atlantic tropical cyclones, *Science*, *325*, 77, doi:10.1126/science.1174062.

Klein, S. A., B. J. Soden, and N.-C. Lau (1999), Remote sea surface temperature variations during ENSO: Evidence for a tropical atmospheric bridge, *J. Clim.*, *12*, 917–932.

Kug, J.-S., F.-F. Jin, and S.-I. An (2009), Two types of El Niño events: Cold tongue El Niño and warm pool El Niño, *J. Clim.*, *22*, 1499–1515.

Kumar, A., and M. P. Hoerling (1998), Specification of regional sea surface temperatures in atmospheric general circulation model simulations, *J. Geophys. Res.*, *103*, 8,901–8,907.

Latif, M., R. Kleeman, and C. Eckert (1997), Greenhouse warming, decadal variability, or El Niño? An attempt to understand the anomalous 1990s, *J. Clim.*, *10*, 2221–2239.

Lau, N.-C., A. Leetmaa, and M. J. Nath (2006), Attribution of atmospheric variations in the 1997–2003 period to SST anomalies in the Pacific and Indian Ocean basins, *J. Clim.*, *19*, 3607–3628.

Le Marshall, J., et al. (2005), Impact of Atmospheric InfraRed Sounder observations on weather forecasts, *EOS, Trans. Am. Geophys. Union*, *86*, 109,115–116.

L'Ecuyer, T. S., and J. H. Jiang (2010), Touring the atmosphere aboard the A-Train,", *Phys. Today*, *63*(7), 36–41.

Livesey, N. J., W. V. Snyder, W. G. Read, and P. A. Wagner (2006), Retrieval algorithms for the EOS Microwave Limb Sounder (MLS) instrument, *IEEE Trans. Geosci. Remote Sens.*, *44*(5), 1144–1155.

Livesey, N. J., et al. (2011), Earth Observing System (EOS) Aura Microwave Limb Sounder (MLS) Version 3.3 Level 2 data quality and description document, JPL D-33509, Jet Propul. Lab., Pasadena, Calif., [Available at http://mls.jpl.nasa.gov/data/datadocs.php].

Luo, Z. J., D. Kley, R. H. Johnson, G. Y. Liu, S. Nawrath, and H. G. J. Smit (2012), Influence of sea surface temperature on humidity and temperature in the outflow of tropical deep convection, *J. Clim.*, *25*, 1340–1348.

Olsen, E. T., S. Granger, E. Manning, and J. Blaisdell (2007), AIRS/AMSU/HSB Version 5 Level 3 Quick Start, report, 25 pp., Jet Propul. Lab., Pasadena, Calif., [Available at http://disc.sci.gsfc.nasa.gov/AIRS/documentation/v5_docs/AIRS_V5_Release_User_Docs/V5_L3_QuickStart.pdf].

Ramanathan, V., and W. Collins (1991), Thermodynamic regulation of ocean warming by cirrus clouds deduced from observations of the 1987 El Niño, *Nature*, *351*, 27–32.

Read, W. G., et al. (2007), Aura Microwave Limb Sounder upper tropospheric and lower stratospheric H2O and relative humidity with respect to ice validation, *J. Geophys. Res.*, *112*, D24S35, doi:10.1029/2007JD008752.

Richter, I., and S.-P. Xie (2008), The muted precipitation increase in global warming simulations: A surface evaporation perspective, *J. Geophys. Res.*, *113*, D24118, doi:10.1029/2008JD010561.

Soden, B. J., and R. Fu (1995), A satellite analysis of deep convection, upper tropospheric humidity, and the greenhouse effect, *J. Clim.*, *8*, 2333–2351.

Stephens, G. L., et al. (2002), The CloudSat mission and the A-Train: A new dimension of space-based observations of clouds and precipitation, *Bull. Am. Meteorol. Soc.*, *83*, 1771–1790.

Stephens, G. L., et al. (2008), CloudSat mission: Performance and early science after the first year of operation, *J. Geophys. Res.*, *113*, D00A18, doi:10.1029/2008JD009982.

Su, H., and J. H. Jiang (2013), Tropical clouds and circulation changes during the 2006–07 and 2009–10 El Niños, *J. Clim.*, *26*, 399–413, doi:10.1175/JCLI-D-12-00152.1.

Su, H., W. G. Read, J. H. Jiang, J. W. Waters, D. L. Wu, and E. J. Fetzer (2006), Enhanced positive water vapor feedback associated with tropical deep convection: New evidence from Aura MLS, *Geophys. Res. Lett.*, *33*, L05709, doi:10.1029/2005GL025505.

Su, H., J. H. Jiang, J. Teixeira, A. Gettelman, X. Huang, G. Stephens, D. Vane, and V. S. Perun (2011), Comparison of regime-sorted tropical cloud profiles observed by CloudSat with GEOS5 analyses and two general circulation model simulations, *J. Geophys. Res.*, *116*, D09104, doi:10.1029/2010JD014971.

Su, H., et al. (2013), Diagnosis of regime-dependent cloud simulation errors in CMIP5 models using "A-Train" satellite observations and reanalysis data, *J. Geophys. Res. Atmos.*, *118*, 2,762–2,780, doi:10.1029/2012JD018575.

Sun, D.-Z., and R. S. Lindzen (1993), Distribution of tropical tropospheric water vapor, *J. Atmos. Sci.*, *50*, 1,643–1,660, doi:10.1175/1520-0469(1993)050<1643:DOTTWV>2.0.CO;2.

Sun-Mack, S., et al. (2007), Integrated cloud-aerosol-radiation product using CERES, MODIS, CALISPO, and CloudSat data, *Proc. SPIE Int. Soc. Opt. Eng.*, *6745*, 1–11.

Tian, B., E. J. Fetzer, B. H. Kahn, J. Teixeira, E. Manning, and T. Hearty (2013), Evaluating CMIP5 models using AIRS tropospheric air temperature and specific humidity climatology, *J. Geophys. Res. Atmos.*, *118*, 114–134, doi:10.1029/2012JD018607.

Waters, J. W., et al. (2006), The Earth observing system microwave limb sounder (EOSMLS) on the Aura satellite, *IEEE Trans. Geosci. Remote Sens.*, *44*(5), 1075–1092, doi:10.1109/TGRS.2006.873771.

Weng, H., K. Ashok, S. K. Behera, S. A. Rao, and T. Yamagata (2007), Impacts of recent El Niño Modoki on dry/wet conditions in the Pacific rim during boreal summer, *Clim. Dyn.*, *29*, 113–129.

Weng, H., S. K. Behera, and T. Yamagata (2009), Anomalous winter climate conditions in the Pacific Rim during recent El Niño Modoki and El Niño events, *Clim. Dyn.*, *32*, 663–674.

Winker, D. M., J. R. Pelon, and M. P. McCormick (2003), The CALIPSO mission: Spaceborne lidar for observation of aerosols and clouds. Lidar Remote Sensing for Industry and Environment Monitoring III, U. N. Singh, et al., eds International Society forOptical Engineering (SPIE Proceedings,Vol. 4893), 1–11.

Zhang, M. H., R. D. Cess, and S. C. Xie (1996), Relationship between cloud radiative forcing and sea surface temperatures over the entire tropical oceans, *J. Clim.*, *9*, 1374–1384.